Measuring Acoustic Fields in an Optical Trap

by

Christopher J. Sarabalis

Submitted to the Department of Physics
in partial fulfillment of the requirements for the degree of

BACHELOR OF SCIENCE

at the

MASSACHUSETTS INSTITUTE OF TECHNOLOGY

June 2014

Signature redacted

Author .....
Department of Physics
May 27, 2014

Signature redacted

Certified by .....
Doctor Sean P. Robinson
Department of Physics
Thesis Supervisor

Signature redacted

Accepted by .....
Professor Nergis Mavalvala
Senior Thesis Coordinator, Department of Physics

Measuring Acoustic Fields in an Optical Trap

by

Christopher J. Sarabalis

Submitted to the Department of Physics
on May 27, 2014, in partial fulfillment of the
requirements for the degree of
BACHELOR OF SCIENCE

Abstract

This thesis describes progress in the use of optical traps for measurement of acoustic fields, a first step toward acoustic micromanipulation in fluids. The optical trap used throughout this study is carefully characterized. Eccentricity of measured distrubitions of thermal fluctuations of trapped dielectric spheres is attributed to a large, directional 60 Hz noise source. Analyses of trap stiffness insensitive to this noise are discussed and their results plotted. Knowledge of the trap and the dynamics of trapped objects are used to make measurements of acoustic fields. Cavity modes are identified and their central frequencies are shown to shift by a part in a thousand over minutes. This change is attributed to the temperature dependence of the speed of sound in the medium. Fluctuations in estimators of cavity mode resonance peak height are shown and the need for acoustic source stability is discussed.

Thesis Supervisor: Doctor Sean P. Robinson
Title: Department of Physics

Acknowledgments

Sean. Andrea. Charles. Joe. Mom. Dad. Nick.

Without you,
I would be
a toaster oven.

Contents

List of Figures

List of Tables

Chapter 1

Introduction

In this chapter, I outline the motivation for this research, placing it in a greater context of similar techniques, and sketch the mechanism underlying the process of measuring acoustic fields with an optical trap.

1.1 Overview of Optical Tweezers and Their Use for Measurement of Acoustic Fields

The use of radiation pressure as a particle trap was first demonstrated by Arthur Ashkin at Bell Labs in 1970 [2]. The first realization of this concept was a counter-propagating, two beam scheme which trapped micron-sized objects. Over the next decade, Ashkin worked to realize a similar concept for atoms. With the innovation of atom cooling and trapping techniques, Ashkin and Chu were able to create the first fully optical atom trap using a single, tightly focused beam in 1986 [5]. Since then optical tweezers have had far reaching impact and are in common use in both atomic and biological physics [7][9].

Intricate models are necessary to quantify precisely the restoring force on micron-sized, dielectric objects toward a near-infrared laser's focus, but the idea is not difficult to physically motivate. In the case where the object's diameter d is much smaller than the wavelength of the trapping light λ, the dielectric simply ascends the electric field

intensity gradient toward the focus of the beam. High numerical aperture (NA) of the beam is necessary for rigid confinement along the axis of the beam. In the opposite scenario, the ray optics regime $\lambda \ll d$, it is most clear to make arguments on the basis of conservation of momentum. If the object deflects the beam along a particular lateral direction perpendicular to the beam axis, the beam's momentum is changed and a corresponding reactionary force must be exerted on the deflecting object. To illustrate the geometry of the restoring nature of such a force, imagine shining a flashlight on a glass of water. Displacing the glass to the left of the beam refracts light to the left and exerts a tiny force equivalent to the rate of change of the light's momentum on the glass to the right. A similar argument can be made for a restoration force along the beam's axis. The need for high numerical aperture becomes once again apparent.

Instead of a glass of water, a 3.2 μm diameter glass (SiO_2) bead is trapped and, in place of a flashlight, a 340 mW, 975 nm wavelength fiber Bragg grating diode laser is used. The bead is trapped in a thin, aqueous environment using an oil immersion microscope to achieve high numerical aperture. After the beam passes through and is deflected by the trapped sillica bead, it is imaged onto a quadrant photodiode (QPD) where its deflection is converted to a voltage and sampled.

An acoustic field is an oscillation of a medium's particle velocity field $\mathbf{v}(\mathbf{r})$. This field is coupled to the motion of the small, spherical bead via Stokes's Law, where the force on the bead $\mathbf{f}$ is equal to $-\beta(\dot{\mathbf{x}} - \mathbf{v}(\mathbf{x}, t))$. Here β is the drag coefficient $3\pi\eta d$ with dynamic viscosity of the fluid η, time t, and bead position $\mathbf{x}$. When sound propagates about the fluid, the fluid vibrates and the bead vibrates in response. This vibration deflects the laser which is then measured on the QPD as a vibration in the voltage. It is by this process that one can measure the acoustic fields in a micron-sized neighborhood of a fluid. By moving the bead around a stationary field, or perhaps using multiple simultaneous traps in a dynamic field, one can generate a map of the acoustic field.

1.2 Motivations for Measuring Acoustics in an Optical Trap

There are two primary motivations for the work described here. The first, being the more direct of the two, is simply measurements of high frequency acoustic fields in fluids with high spatial resolutions. Particularly the aim is to measure the acoustic field without significant disruption. The second motivation is the use of optical tweezers for the characterization of acoustic micromanipulation techniques.

There are highly powerful and widely used techniques for the employment of acoustics to measure microscale features, namely scanning acoustic microscopes. These techniques rely on confocal imaging to achieve high resolution maps of the acoustic impedance of a sample. To this end, the use of optical tweezers for acoustic measurements is not likely to surpass the practicality and speed of scanning acoustic microscopy. With one optical trap, each point in space needs to be scanned individually and scanning speed is limited by trapping strength: moving too fast will cause objects to fall from the trap. The potential utility of the optical tweezer modality is not in imaging acoustic impedance across a particular sample, but in studying complex, potentially nonlinear acoustic scattering in media such as biological tissues. The size of the scatterer being used in the optical tweezers cause little disturbance of the field, and fine control of the trap's location grants spatial resolutions limited only by staging capabilities and the trap's size. Most importantly, the use of optical tweezers for the measurement of acoustic fields does not constrain the shape of incoming driving fields. For these reasons, this acoustic field imaging modality is aimed at creating a sandbox for the study of nonlinear acoustics in complex media.

The second primary motivation for studying acoustics using an optical trap is to lay the groundwork for the characterization of acoustic micromanipulation of objects in fluid media. Large strides have recently been made in the realm of acoustic control of objects in air using ultrasound [8]. This work has demonstrated 3 dimensional spatial control of millimeter-scale objects. Furthermore, theoretical work has shown the ability for acoustic Bessel beams to trap polystyrene spheres [3]. Extending

the micromanipulation techniques in air to fluid media or implementing the Bessel beam traps of Baresch *et al.* [3] could provide a micromanipulation tool much akin to optical tweezers but potentially escaping constaints on sample thickness, sample optical characteristics, and trapped object geometry. If acoustic micromanipulation techniques could be realized and well understood in complex media, such a tool could perhaps be used for therapuetic means in living tissues.

There are many steps to be taken toward the realization of acoustic tweezers or the investigation of the feasibility of *in vivo* micromanipulation. Likely the first landmark is the extension of the ultrasonic standing wave trapping techniques implemented in air to water. In its simplest incarnation, a standing wave is created in one dimension using a single transducer and reflector, and objects are trapped in velocity nodes of the acoustic field. In more complex arrangements, objects are transported around by manipulating the locations of the velocity nodes. The goal is to generalize to arbitrary arangements of transducers spanning a boundary, for example, wrapping an inhomegnous medium of interest in a film of acoustic transducers. One can imagine that rather than wanting to move a bead about (translate a point velocity node), instead wanting to press on or translate a surface. Using arrangements of transducers that bound the space of interest could allow for the creation of standing waves with more complex geometries and more flexible control. Left to be answered – and likely requiring a computational approach – would be how a particular transducer geometry limits the possible manipulation maneuvers, or achievable acoustic fields.

A simultaneous branch of possible questioning concerns scattering and manipulation in inhomogenous fields. The problem breaks down into imaging the impedance across a medium and using an understanding of the medium to exert localized or trapping forces. Using a transducer array across a bounding surface of a region of interest to image the region via scattering can be formulated as an inverse scattering problem with information on asymptotic field states specified by a particular transducer geometry. These types of inverse scattering problems are actively studied in the field of seismology. For this investigation, scanning acoustic microscopy could be used as a check on progress and the optical trap could allow for imaging of the

acoustic field within the body of the medium (so long as one is restricted to thin, transparent samples). Such an approach yields an advantage over typical seismological studies which use only transducers across a piece of the bounding surface. After mapping a medium, one might then compute and create acoustic fields for particular manipulative maneuvers which can then be checked using an optical trap. It is this prospect of the optical trapping technique for measuring acoustic fields – to image small-wavelength ultrasonic fields throughout the body of a thin fluid medium, that could fuel research into acoustic micromanipulation – that motivates this work.

With this in mind, I verify that acoustic fields can be measured using an optical trap, study the technological and physical limitations of such an approach, and use the trap to find standing waves in an acoustic cavity.

1.3 The Physics of Optical Trapping and Acoustic Disturbances

With measurements of a trapped silica bead's trajectory $\mathbf{x}(t)$, a model of the bead's dynamics is needed to compute the evolution of the local acoustic field. For small driving forces, objects explore a region of the optical trap that is well approximated by a harmonic potential (this will be experimentally justified in Chapter 2). In general the trap is elliptical (due to eccentric output of the optical system) and can be expressed in terms of perpendicular stiffness vectors $\mathbf{k}_1, \mathbf{k}_2$ that lie along the semimajor and semiminor axes of the trap. The equation of motion is

$$m\ddot{\mathbf{x}} + \beta\dot{\mathbf{x}} + \left(\sum_i \hat{\mathbf{k}}_i \mathbf{k}_i \cdot\right)\mathbf{x} = \beta\mathbf{v} + \mathbf{g}(t). \tag{1.1}$$

For low Reynolds number $\mathrm{Re} \equiv \frac{\rho v d}{\eta}$, where η is the dynamic viscosity and ρ is the density of the fluid, the drag force on the bead is related to the particle's relative velocity to the flow by Stokes's Law

$$\mathbf{f}_{\mathbf{drag}} = -3\pi\eta d\,(\dot{\mathbf{x}} - \mathbf{v}) = -\beta.(\dot{\mathbf{x}} - \mathbf{v})\,. \tag{1.2}$$

In Equation 1.1, we move the component due to the fluid particle velocity $\mathbf{v}$, as determined by the acoustic equations of state, to the right hand side. For acoustic fields of wavelength $\lambda \gg d$ (I encounter wavelengths no smaller than a millimeter), spatial variations in $\mathbf{v}$ are negligibile in computing the dynamics. In addition to viscous and trapping forces, we have thermal fluctuations modeled as schostatic process $\mathbf{g}(t)$ with white noise spectrum of amplitude $4\pi k_B T$ [6]. Given a trajectory $\mathbf{x}$ and knowledge of the trap $\mathbf{k}_1, \mathbf{k}_2$, we can directly compute $\mathbf{v}$ up to an uncertainty from thermal fluctuations.

Before continuing with a spectral analysis, I'll discuss the relevant scales in the experiment to come to justify the need for a spectral approach to separate the effects of noise as opposed to a direct calculation of $\mathbf{v}$ using Equation 1.1. I am trapping sillica spheres with densities of 2.65 $\frac{\mathrm{g}}{\mathrm{cm}}$ and average mass of 45.5 pg. Viscous forces are set by $\beta = 0.0282\ \frac{\mathrm{pN}}{\mu\mathrm{m/s}}$. Achievable stiffnesses in our slightly trap are $\approx 10\ \frac{\mathrm{pN}}{\mathrm{m}}$ to 50 $\frac{\mathrm{pN}}{\mathrm{m}}$. Under constant acceleration, the bead reaches its terminal velocity on a timescale of 1.6 μs. For low frequency driving forces, the bead behaves like a first order filter with roll off beginning at $\omega_c = k/\beta$ which is about $2\pi \times 300$ Hz for the stiffest achievable trap in our setup. I will ultimately be interested in driving the bead at ultrasonic frequencies which are heavily damped out by the bead's dynamics. Thermal responses at low frequences where they are not suppressed by the bead's dynamics dominate $\mathbf{x}$, but a spectral analysis can be used to remove these obscuring effects.

Coordinate path functions $x_i(t) = \hat{\eta}_i \cdot \mathbf{x}(t)$, $v_i(t) = \hat{\eta}_i \cdot \mathbf{v}(t)$ and constants $k_{ij} = \hat{\eta}_j \cdot \mathbf{k}_i$ are used to represent $\mathbf{x}, \mathbf{v}, \mathbf{k}_1, \mathbf{k}_2$ in terms of their components along the QPD axes $\{\hat{\eta}_1, \hat{\eta}_2\}$. Performing a Fourier transform (convention $\int \mathrm{d}t\, e^{i\omega t}$) on Equation 1.1 yields

$$\left[\left(-m\omega^2 + i\beta\omega\right)\mathbf{I} + \mathbf{K}\right]\tilde{\mathbf{x}} = \beta\tilde{\mathbf{v}} + \tilde{\mathbf{g}}. \tag{1.3}$$

We've expressed the linear operations in Equation 1.1 in terms of the identity matrix $\mathbf{I}$ and the stiffness matrix $\mathbf{K}$ with basis vectors along the QPD axes. We can solve for $\tilde{\mathbf{v}}$, apply a filter $F(\omega)$ to eliminate the effects of noise at low frequencies, and multiply

each side by its complex conjugate. That leaves an expression for the filtered power $< \mathbf{v}^2 >_F$

$$\beta^2 \left\langle \mathbf{v}^2 \right\rangle_F = \left\langle \xi^2 \right\rangle_F - 4\beta k_B T \int \mathrm{d}\omega F(\omega), \tag{1.4}$$

where

$$\left\langle \xi^2 \right\rangle_F = \frac{1}{2\pi} \int \mathrm{d}\omega \bar{\xi}(\omega) F(\omega) \xi(\omega) \tag{1.5}$$

and

$$\xi = \left[\left(-m\omega^2 + i\beta\omega \right) \mathbf{I} + \mathbf{K} \right] \tilde{\mathbf{x}}. \tag{1.6}$$

In this way we can isolate the effects of the transducer and measure $< \mathbf{v}^2 >$ from acoustic driving limited only by statistical fluctuations in the thermal process in the band of interest and the precision of the QPD.

Up to this point we have specified the characteristics of the bead and fluid in our setup through m, β, η but have left unspecified unconstrained degrees of freedom associated with the optical trap. In the setup discussed in Chapter 2, the stiffness of the trap can be adjusted by adjusting the laser current. What is the best choice of current to maximize the sensitivity of our apparatus? If we simplify our model to a 1D case (which works well for low trap eccentricity) and ignore thermal effects we have

$$\left\langle \mathbf{x}^2 \right\rangle_F = \frac{\beta^2 \left\langle \mathbf{v}^2 \right\rangle_F}{\left(k - m\omega^2 \right)^2 + \beta^2 \omega^2}. \tag{1.7}$$

Minimizing the denominator over the 1D trap strength k, the undamped resonance frequency of the trap is set to the driving frequency by adjust the trap stiffness to $k = m\omega^2$. For a typical trapping strength of 10 pN/μm, we find a corresponding driving frequency of 2.36 kHz. Our maximum achievable stiffness of 50 pN/μm yields a peak sensitivity around 5.27 kHz. For most driving frequencies of interest, we will operate at maximum trap stiffnes/laser current. If we are interested in $\omega_{\mathrm{drive}} = 2\pi \times 20$ kHz, the relevance of the trapping stiffness in the bead dynamics dwindles to $\frac{k}{m\omega^2} = 7\%$. Measurements of higher driving frequencies are less dependent on careful characterization of the stiffness of the optical trap. If errors in the determination of the stiffness of the trap is stiffness dependent, one can trade sensitivity (the size of

the denominator in Equation 1.7) for knowledge of the characterization of the trap.

Chapter 2

Characterizing the Optical Trap

In this chapter the details of the optical trapping apparatus and calibration measurements are discussed. I start by outlining the apparatus, discussing the components leading to limitations on acoustic measurements. I then present calibration measurements used for position detection of trapped objects. I end with the various means of measuring trap stiffness which are presented and compared.

2.1 Apparatus

A schematic of the trapping apparatus is given in Figure 2-1. Our trap's design is based on that presented by Appleyard, Vandermeulen, and Lang and is available as a kit from Thorlabs [1]. It is a single beam 1064 nm setup in which the trapping beam is directly imaged onto a quadrant photodiode (QPD) for position detection of trapped objects. Visible light is counterpropagated through the sample through hot mirrors that guide the trapping light, and collected by a CCD. Samples are fixed to a 3D piezoelectric stage and coarsely position with micrometers. The piezoelectrics are in closed-loop with strain gauges for stage position control and measurement. Oil immersion microscope objectives are used to achieve high numerical aperture (NA).

Two components of the apparatus set the upper limits on measurable frequencies for acoustic signals. These upper bounds on frequency set lower bounds on acoustic wavelengths that limit the scale of interesting imagable features well above the

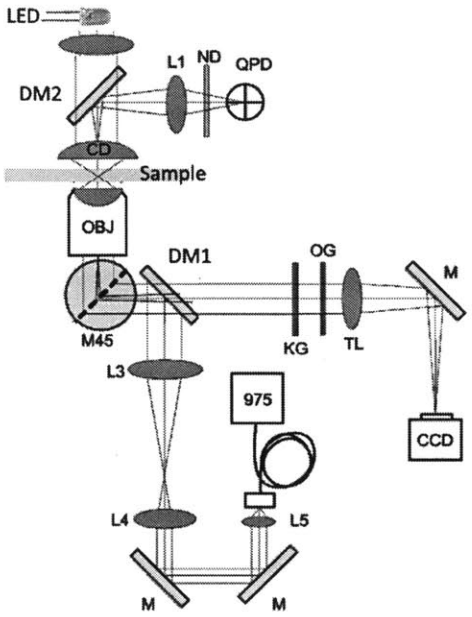

Figure 2-1: Schematic of the Optical Trap. This diagram, with minor modifications, is from Appleyard *et al.* [1].

physical limitation of trap size and the technical limitation imposed by stage position precision. The first major limitation in our setup is simply the maximum sample rate of our data acquisition system of 100 kHz. Our apparatus is thereby capped at 50 kHz Nyquist frequency. The second limitation on bandwidth is time constants intrinsic to the position detection device. Our QPD's response is rated to fall of at approximately 10 kHz. This falloff was explained by Berg-Sørensen in 2003 in terms of a two component response in the silicon to incident infrared light [4]. If electron-hole pairs are generated within the depletion zone of the silicon detector, the detector's response is fast. But longer wavelength incident light generates electron-hole pairs outside the depletion zone which slowly diffuse into the depletion region before fast transport to the detector's electrodes. Attempts to correct out this parasitic filtering are complicated by the wavelength and amplitude dependent nature of the phenomenon. A detailed study of these effects are presented by Peterman *et al.* [10]. Rather than endeavor to correct out the effects of the parasitic filtering in an attempt to acquire reliable absolute magnitudes, I focus on exploring the bounds of sensitivity of the technique.

There are silicon detectors on the market which offer an order of magnitude greater bandwidth. Another means of achieving higher bandwidth is the use of a separate probe laser at a wavelength more easily absorbed by conventional silicon detectors.

Optical traps are readily susceptible to mechanical noise. Such noise is readily apparent in power spectral densities of a trapped object's position as in Figure 2-6. These noise sources obscure measurements of low frequency acoustic fields. We are principally concerned with fields with wavelengths on the centimeter or millimeter scale with corresponding frequencies well beyond these sources of noise. However these noise sources do contribute directly to measurements of the trap's stiffness via the equipartition theorem as described in Section 2.3.1.

Limitations on sample thickness are rooted in the optics of optical tweezers. High numerical apertures are necessary to maintain sufficient trapping forces along the beam's axis. As the beam is transmitted from the immersion oil to the fluid medium, the resulting refraction causes spherical aberration increasing in severity as the focus is moved away from the coverslip at the bottom of the sample. Our trap becomes axially unstable at around 150 μm.

2.2 Mapping QPD Voltages to Bead Position

Voltage signals are converted to position by measuring beam deflection for known displacements of the piezoelectric stage. Beads are diluted in a 1M NaCl solution and allowed fives minutes to fix to the coverslip of a flow channel. The channel is then reflowed with deionized water to avoid discrepancies in the index of refraction of the medium. To reflow the channel, a droplet of deionized water is placed at one end of the channel and a tissue is placed at the other. During this process, many beads dislodge and are deposited at the tissue end of the channel. The channel is then sealed with VALAP.

Calibration is done by sweeping across the bead along each lateral stage axis in turn and recording the the response. The resulting traces in QPD X and QPD Y voltage space are plotted and analyzed in real time. If the bead is being swept off

center, that is if the center of the laser is not moving through a plane that intersects the bead's center, the QPD trace exhibits a curvature. When the bead is swept through the center (through a plane of symmetry of the bead), the laser is deflected along the axis of the sweep and the QPD trace is straight. The stage is adjusted along an axis perpendicular to the sweep until the center is found. The QPD is rotated to align the QPD X-axis to the X-axis of the stage. Data is collected along each stage axis for various laser currents.

Not all beads that appear to be stuck to the coverslip will trace a straight line. Some beads will trace messy elliptical shapes regardless of centering. In practice a few beads must be checked before finding a suitable one. This recalcitrance may be a result of variation in the degree to which the beads are stuck.

If all beads were the same size, one calibration run over the range of currents would suffice. Variation in bead diameter necessitates running the calibration over a sample of well stuck beads. It is not possible to use a bead for calibration and then unstick it for use in measurements.

Figure 2-2 is a plot of the beam deflection as measured by the QPD against the stage position for a particular bead and laser current. The sweep is well beyond the linear regime of the trap and shows regions adjacent to the main trapping region that actually repels the object (reversed slope). As laser current is varied, the curve in Figure 2-2 is scaled proportionally with the beam's intensity. As we have no measurements of the beam intensity, the calibration process is performed over multiple currents.

The QPD and stage strain gauges are sampled at 10 kHz over 10 s. The stage oscillates over 16 μm at 0.5 Hz such that each run is averaged over 10 sweeps of the bead. The data (shown as light blue points) are then sorted into 150 equal-width bins (plotted as dark blue points and candles) along the axis describing stage position. Least chi-square linear regressions are performed to the linear regions plotted in red in the left of Figure 2-2. The slope of this fit is then used to convert QPD voltage into bead position. This process works well for small bead displacements from the trap's center, as is the case for the deflections of interest. For measuring static forces

such as on single molecules, more general regressions are performed [9].

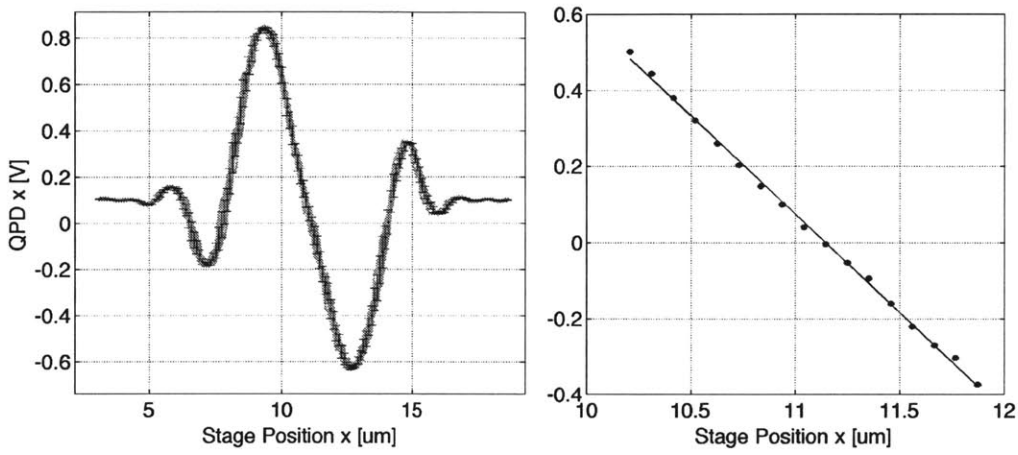

Figure 2-2: Linear Regression for Calibration Coefficient for a Particular Bead, Current, and Direction. A fixed bead is swept through its center. Data is collected into evenly spaced bins by stage positions. A linear fit, shown at right, is performed to data in the linear region of the curve at left. A plot of QPD X against stage position shows not only a dominant trapping region but also a surrounding series of increasingly weaker repelling and trapping regions.

The error of the calibration is dominated by variation in bead diameter. For a particular bead, as current is varied the regressed calibration slope varies quite linearly (Figure 2-3). Comparing various beads yields markedly different slopes. As the variation is in the slope, larger currents result in greater variation in predicted calibration coefficient. In addition to errors from bead diameter variance, there is "X-Z crosstalk": as the position of the focal plane is moved along the beam's axis from the center of the fixed bead, the calibration coefficient varies. The focal plane sits below a trapped object (due to pressure from reflected light), but scattering from the coverslip prevents duplication of this arrangement during calibration. Furthermore the distance between the bead and the oil/water interface could affect calibration coefficient. It is possible to use beam intensity measurements to accurately measure the bead's axial position and take into account these effects [9].

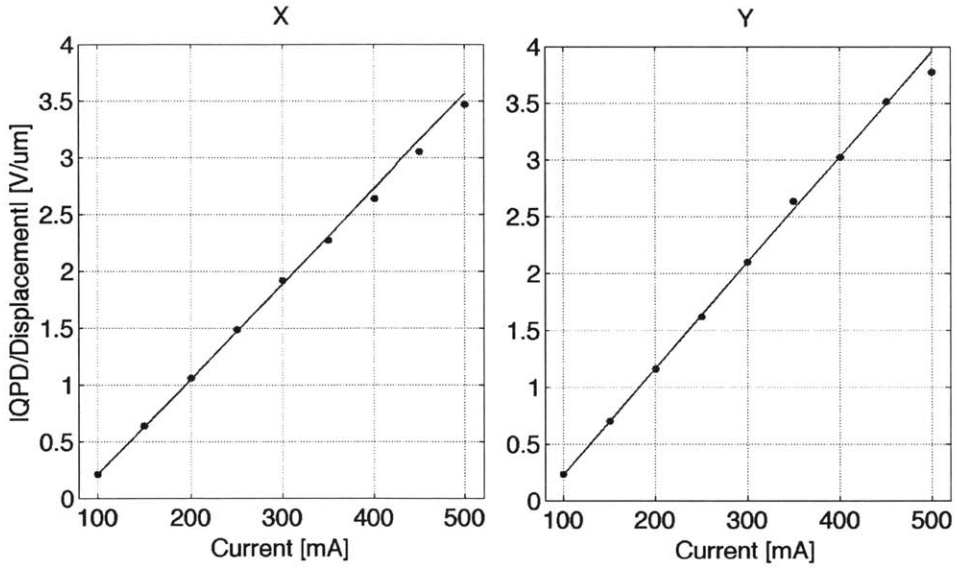

Figure 2-3: Calibration Coefficient over Current for a Single Bead. If the same bead is used across laser current, the change in calibration coefficient with current is highly linear for both axes. The dominant uncertainty in calibration of data is the variation that comes about from uncertainty in the diameter of the bead.

2.3 Measuring the Stiffness of the Trap

Two types of measurements are made in order to determine the trap stiffness matrix **A**. The first is measurements of thermal fluctuations of the bead's position. The statistics of these fluctuations are used to characterize the optical trap. The second is measurements of the bead's response to coupling of the fluid particle velocity field. Translational control of the stage is used to apply known Stokes drag forces and deviations of the bead are used to compute stiffness.

In this section I discuss the eccentric statistics of thermal fluctuations and show that this eccentricity is a result of directional 60 Hz noise. I then compare the various methods for characterizing a circular trap: the equipartition theorem and spectral analyses of thermal fluctuations; and variance-based and fit-based analyses for the driven measurements.

2.3.1 Stiffness from Thermal Fluctuations

There are a few methods by which the trap's stiffness can be computed from measurements of thermal fluctuations, some of which utilize statistical information about the bead's trajectories, and the other being a spectral analysis informed by our model of the bead's dynamics. To measure the thermal fluctuations in the bead's position, a flow channel is prepared with beads in deionized water; a bead is trapped and placed 15 bead diameters from the bottom coverslip to avoid viscous interactions described by Faxen's law.

The statistics of a particle's position in an eccentric two dimensional harmonic potential in a canonical ensemble are described by

$$p(x,y) \propto \exp\left(-\frac{k_1(\hat{k}_1 \cdot \mathbf{x})^2 + k_2(\hat{k}_2 \cdot \mathbf{x})^2}{2k_\mathrm{B}T}\right). \tag{2.1}$$

The statistics along each axis are independent of the other. The functional form above is just a bivariate normal distribution. In general the axes of the stiffnesses will lie off the axes of the QPD and the stage. One can use the covariance to compute this angle and rotate into a basis along the stiffness vectors:

$$\tan(2\theta) = \frac{\sigma_{x,y}}{\sigma_x^2 - \sigma_y^2}, \tag{2.2}$$

where x and y are coordinates in the QPD basis, and θ is the angle by which the stiffness basis is rotated from the QPD basis. Sigma on the right hand side of Equation 2.2 denotes the second cummulants of the probability distribution. After rotating into the stiffness basis, the equipartition theorem can be used to compute the stiffness of the trap. The equipartition theorem states that the average energy for each independent quadratic degree of freedom in the Hamiltonian contributes $k_BT/2$ to the average energy of the system. From this we have

$$k = \frac{k_\mathrm{B}T}{\langle x^2 \rangle}, \tag{2.3}$$

where k is the trap stiffness along the X-axis and $\langle x^2 \rangle$ is the second moment of the distribution along that axis. Figure 2-4 is a contour plot of a histogram for a typical run (laser current 179 mA). Contours are separated by 2500 counts.

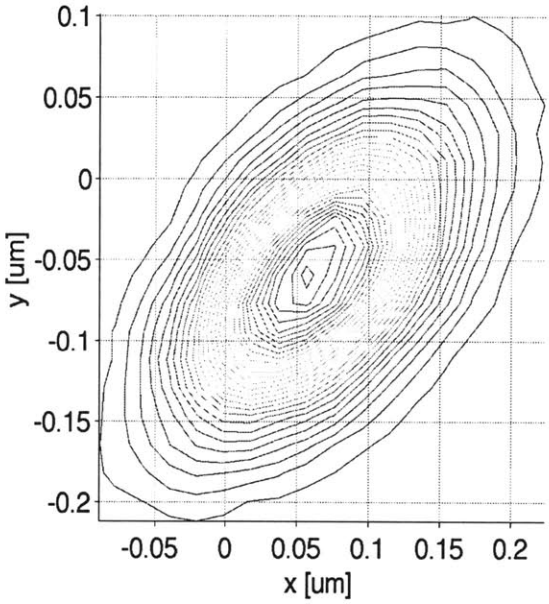

Figure 2-4: Histogram of Bead Thermal Fluctuations before Rotation. Histograms of the bead's position over thermal fluctuations are highly gaussian and very eccentric. Furthermore the eccentricity does not align with the stage/QPD axes. The data can be rotated into new coordinates in order to eliminate the X-Y correlation and simplify further analyses.

The histogram shown above is clearly eccentric and off-axis, having a Pearson correlation coefficient $\rho = 0.4$. Varying by only a couple degrees across laser currents, the resulting angle θ is 23°.

The QPD was sampled at 6 kHz for 60 s incrementing laser current by 50 mA between 100 and 500 mA. Rotation angles are computed for each laser current, the basis axes are rotated, and the stiffness is computed by Equation 2.3. Results are plotted in Figure 2-5. The second moment along the quadrant photodiode's X-axis which corresponds to the thin lateral axis of the flow channel is larger than the second moment along the Y-axis, resulting in lower computed trap stiffnesses.

It is left then to evaluate whether eccentric statistics imply an eccentric trap. If

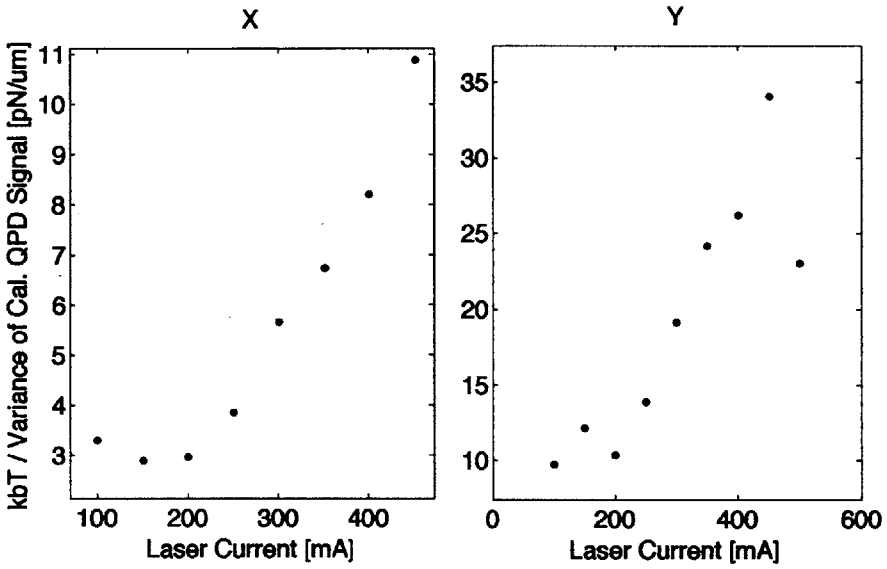

Figure 2-5: Trap Stiffness via Equipartition Theorem. The variance of the bead's position over thermal fluctuations is used to compute the stiffness along axes rotated to eliminate X-Y correlation. The rotated X-axis plotted at left yields trap stiffnesses about 3 times smaller than those computed for the rotated Y-axis.

one only had access to the statistics of the bead's location, this might be a tempting conclusion. I perform a spectral analysis on the same data set to check this notion.

For the undriven situation (quiescent medium), the fluid velocity can be set to zero $\mathbf{v} = 0$ in Equation 1.3 to get

$$\left[\left(-m\omega^2 + i\beta\omega\right)\mathbf{I} + \mathbf{A}\right]\tilde{\mathbf{x}} = \tilde{\mathbf{g}}. \tag{2.4}$$

Along a single rotated axis, the trap stiffness matrix A is replaced by a scalar k. Solving for $\tilde{x}$ and computing the squared modulus

$$\tilde{x} = \frac{4\pi k_{\mathrm{B}}T}{\left(k - m\omega^2\right)^2 + \beta^2\omega^2}, \tag{2.5}$$

where the Wiener process has been replaced by its spectrum $4\pi k_{\mathrm{B}}T$. For low frequencies $k \gg m\omega^2$, the inertial term is dropped from the denominator of Equation 2.5. Trap stiffness is then determined by the location of the roll-off $\omega_{\mathrm{c}} = k/2\pi\beta$.

For each axis along each run, we take the product of the single-sided discrete

Fourier transform with its complex conjugate shown on a log-log plot in Figure 2-6 for 200 mA. Raw transformed data are plotted in light gray. The 180,000 points are

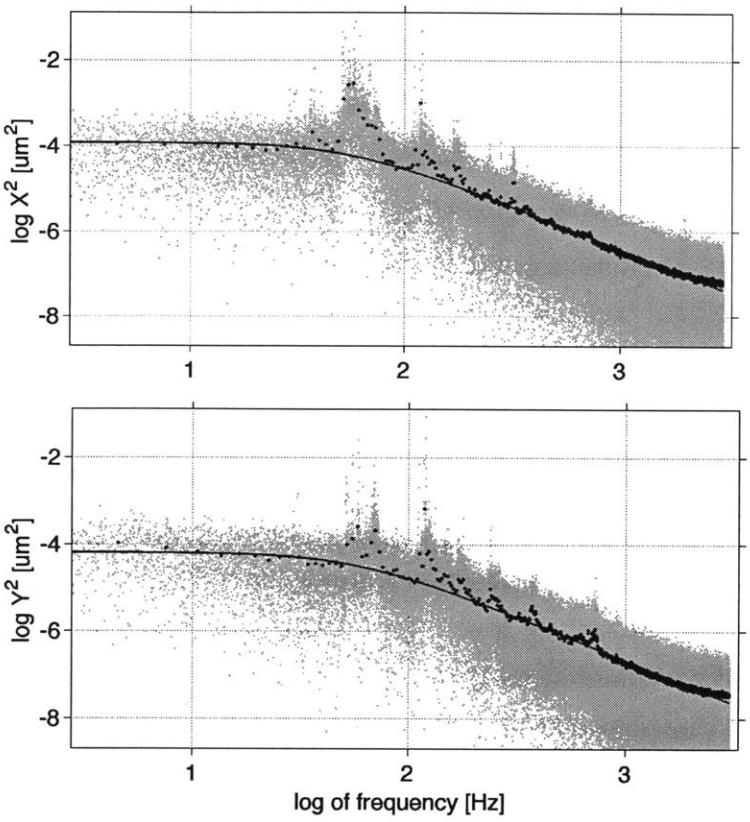

Figure 2-6: Spectral Analysis: Evidence of Directional Noise. Discrete Fourier transforms (DFTs) are performed on calibrated and rotated data sets in which the bead is trapped in a still medium. The data are then binned and fit to a Lorentzian to compute trap stiffness. The top plot is a $\log_{10}$-$\log_{10}$ spectrum along the rotated X-axis; the bottom plot is along the rotated Y. The large 60 Hz noise peak is rotated by the means explained in this chapter along the X-axis, causing equipartition results to yield lower stiffnesses in this direction. Spectral methods are less sensitive to noise peaks than equipartition methods.

put into 1,000 bins. The averages of these bins are plotted in dark gray. Error bars are ommitted for clarity. The means and standard deviations of this binned data set is used to perform a fit to a Lorentzian:

$$f(x) = \frac{a_1}{a_2^2 + x^2}. \tag{2.6}$$

The fit coefficient a_2 is then used to compute the trap's stiffness for a given current.

Comparing the two power spectral densities along the rotated axes answers this question of eccentricity. In the spectral analysis of motion along the X, or loose, axis, we have a large noise spike at 60 Hz. Not to be confused by the logarithmic scale of the plot, this noise peak has a significant impact on the motion of the bead and the statistics of its trajectories. The results plotted below show that the stiffness as computed by the spectral analysis yields similar results despite the discrepancy predicted by the equipartition method. Ultimately the equipartition method indiscriminately captures all power, noise or not, whereas the power spectral density approach is more insensitive to noise spikes. For the PSD, noise spikes below the shoulder work to push the shoulder's roll-off to lower frequencies, or lower stiffness. Noise spikes to the right of the shoulder do just the opposite. These systematics help to explain the discrepancy between trap stiffnesses along the X and Y-axis. As seen in Figure 2-6, the X data have large noise to the left of the shoulder and the Y data have more noise to the right of the shoulder. But these systematics are much smaller than in the equipartition analysis chain. The eccentricity of the equipartition analysis and the histogram plotted in Figure 2-4 is the result of a directional source of environmental noise.

The results of the fits over laser current is shown in Figure 2-7. Stiffnesses computed via spectral analysis are similar across currents along both axes. Differences between data are greater than what can be explained by unplotted propagated statistical variation within bins. The anticipated systematic effects of the different noise along each direction help to explain the consistently higher stiffness computed along the Y-axis. I next discuss a driven method for measuring the trap stiffness and finally summarize the process of trap characterization.

2.3.2 Stokes Drag Stiffness Measurements

Rather than using measurements of the bead's response to thermal fluctuations to characterize the trap, we can drive the bead via Stokes drag using the v term on the right hand size of Equation 1.3. By driving the bead hard enough with a known

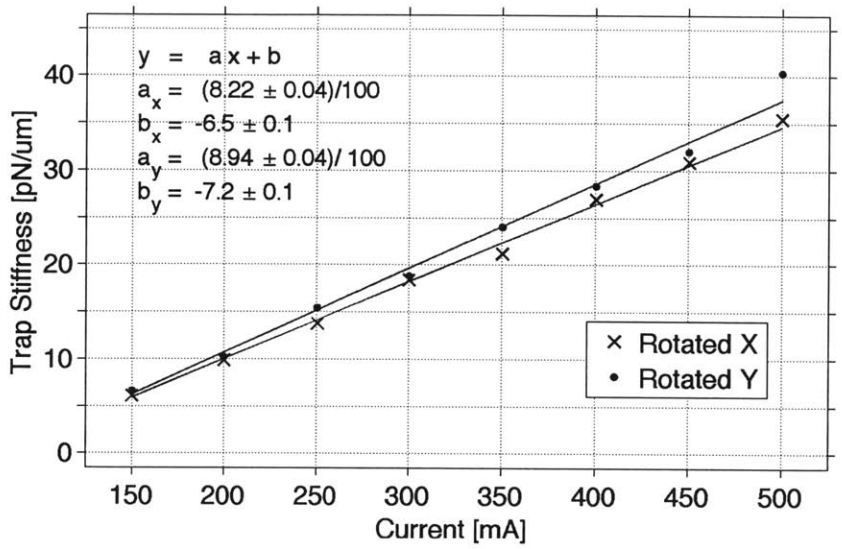

Figure 2-7: Stiffness by Spectral Analysis over Current. Results from the spectral approach along the X and Y-axes are plotted above with linear fits. Deviations from linearity and discrepancies between the axes fall beyond what is accountable for statistical uncertainty propagated from the binning through the fitting procedure. Uncertainties are likely dominated by variations in temperature within the sample.

velocity field $\mathbf{v}$ that varies in time slowly (driving period much less than the time it takes the bead to reach terminal velocity which is about 1μs), we can ignore Wiener process $\mathbf{g}$ and inertial term $m\omega^2$, giving

$$kx = \beta(v - \dot{x}). \tag{2.7}$$

In Equation 2.7, we have assumed that the trap is circular as evinced by the spectral analysis in the preceding section and projected the vectors along the driving axis. For a discrete jump in the local fluid particle velocity $\mathbf{v}$, the bead exponentially reaches some equilibrium position over a time scale of β/k. For a weak 100 mA trap, this corresponds to a decay time of 2 ms. As long as we vary the fluid velocity slower than 500 Hz, we can drop the $\dot{x}$ term from Equation 2.7.

The same bead trapped 15 bead diameters above the coverslip used for the thermal fluctuation measurements is then driven using the piezoelectric stage sinusoidally with an amplitude of 8 μm at 0.75 Hz for 100 mA, 1.0 Hz for 150 mA, and 1.5 Hz for larger

laser currents. Data was collected at 6 kHz for 60 s.

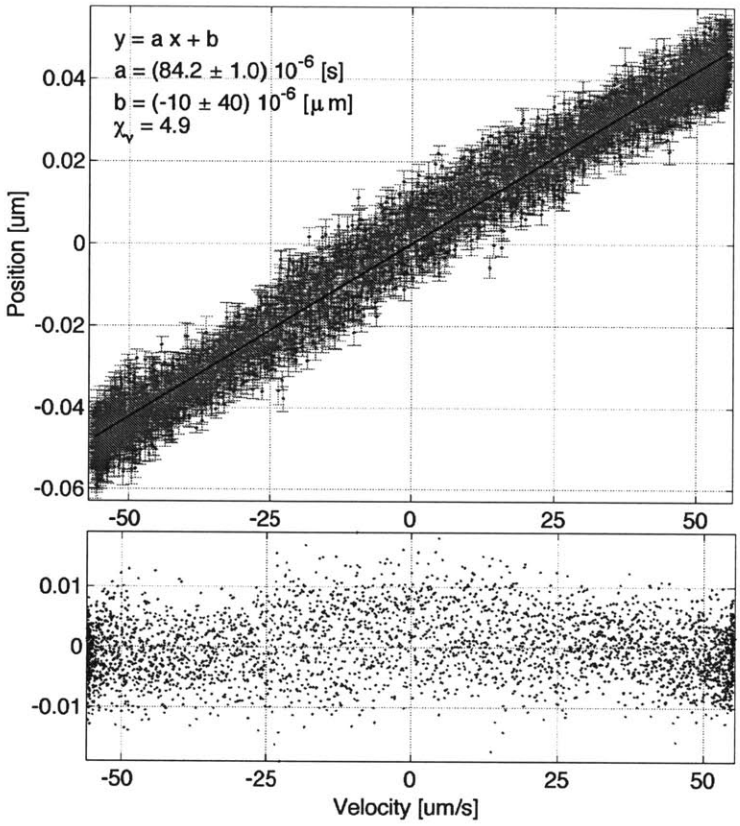

Figure 2-8: Stokes Drag Fit-Based Analysis. The data from Stokes drag measurements are binned: effectively downsampled. A finite difference is used to compute stage velocity from strain gauge data and it is plotted against QPD bead position data. These points are then fit to a line, the fit parameters of which are used to compute trap stiffness. The lower panel shows unstructured residuals.

Two means of computing the trap stiffness were used. The first was to take the ratio of the the second cumulant of the bead's position along the driven access, computed from the data, and the second cumulant of the stage velocity, computed from settings. The root of this ratio gives the ratio between k and β.

The second means was to directly compute from strain gauge and QPD data the position and stage velocity and perform a linear fit to the data. The time series data are collected into bins of 100 consecutive points. The velocity of the stage is computed by finite difference and divided by the time between binned averages. Bead

position is plotted against velocity and a linear fit is performed using the averages and standard deviations of the bins. This process is repeated for currents between 100 and 500 mA with 50 mA spacing. Figure 2-8 shows the fit process and residuals for a run at 450 mA.

Results of the two analysis methods are shown in Figure 2-9. The variance analysis method yields consistently higher stiffnesses than that of the fit method.

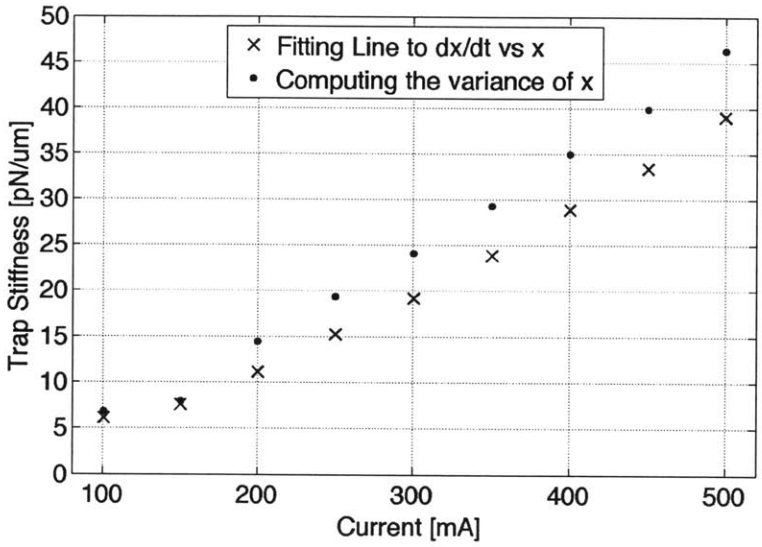

Figure 2-9: Stiffness via Stokes Drag over Laser Current. A bead is trapped and the stage to which the sample is secured is driven sinusoidally. The bead's position exponentially decays to steady state in negligibly small times where trapping forces balance Stokes drag (Equation 2.7). Two analysis approaches are taken with the blunter of the two, the variance-based method, yielding consistently higher trap stiffness.

2.3.3 Summary of Trap Characterization

Although the eccentric statistics shown in histograms like Figure 2-4 and the results of the rotated equipartition theorem (Figure 2-5) could be explained by eccentricity of the trap, spectral analyses like Figure 2-6 show that this results from a large, directional 60 Hz noise source in the signal chain. Results of spectral analyses (Figure 2-7) show that the trap is nearly circular. Stokes drag analyses are performed

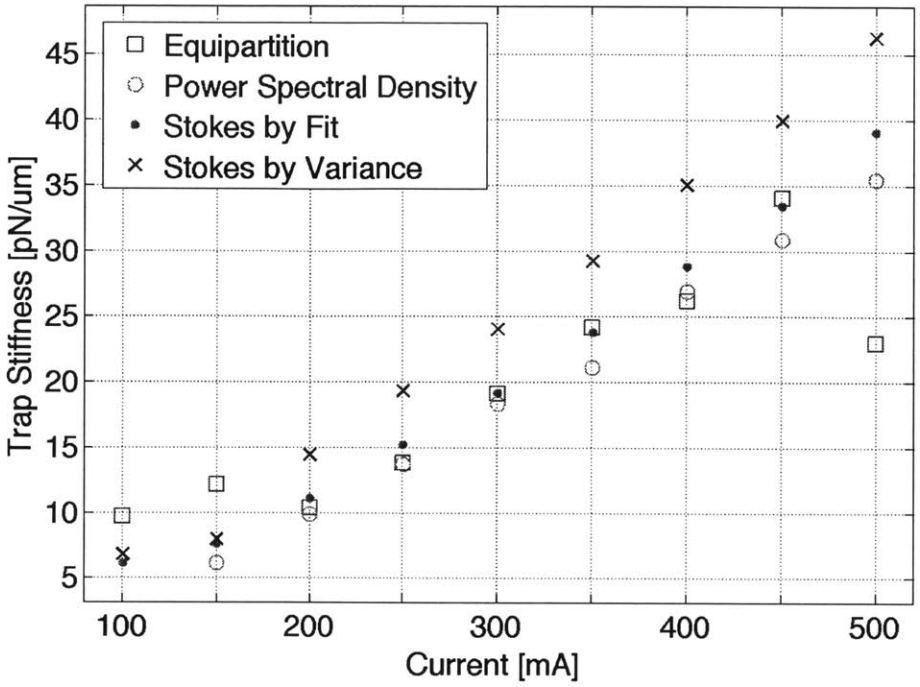

Figure 2-10: Trap Characterization Results for Different Measurements and Analyses. This plot summarizes the results from thermal and stage-driven measurements of the trap stiffness for the various analysis methods employed. The results are largely consistent, excepting an outlying 500 mA equipartition point and the variance-based Stokes drag test. The measurements and analysis chains are described throughout this chapter. These stiffnesses are used to compute fluid particle velocity fields in the following chapter on acoustic measurements.

and analyzed using two methods: a variance-based analysis and a fit-based analysis. The collected results are plotted in Figure 2-10.

With the exclusion of the outlying 500 mA point, the stiffness as measured and computed for the equipartition along the Y-axis, the power spectral density, and the fit-based stokes drag techniques agree within $\pm 3\text{pN}/\mu\text{m}$. The variance-based stokes method on the other hand deviates from these significantly. For the acoustic measurements to follow, we exclude the variance-based Stokes method and the outlying equipartition point when interpolating trap stiffness for various laser currents.

Chapter 3

Measuring Acoustic Fields

3.1 Apparatus

Having described the optical trap, I now describe the acoustic cavity. The construction of our optical trap limits the size of samples. The thickness of the sample is constrained by the distance between the microscope objectives. Additional space must be left between the sample and objectives to setup the oil-immersion microscope and maneuver trapped objects about the cavity. The cavity was milled into a $\frac{3}{16}$ inch thick sheet of steel. It was not until this cavity was created that I found our trap becomes axially unstable due to spherical aberration at around 150 μm or 6 thousandths of an inch. That leaves an unused 181.5 thousandths of an inch. The thickness of the cavity made it very unwieldy during preparation and loading into the trap.

Figure 3-1 is a picture of the prepared cavity. Dimensions of the cavity were selected with standing waves in mind. It was built such that the first and second acoustic mode along the length of the channel would be measurable frequencies given the limitations set by our data acquisition system (50 kHz). The length and width of the cavity are 1.648 and 0.781 inches, respectively. These oddly specific lengths were selected in early stages while entertaining notions of using eddy currents in a thin cavity wall to create standing waves with 100 μm wavelengths. This idea was abandoned due to the frequency constraints imposed by the detector, but the

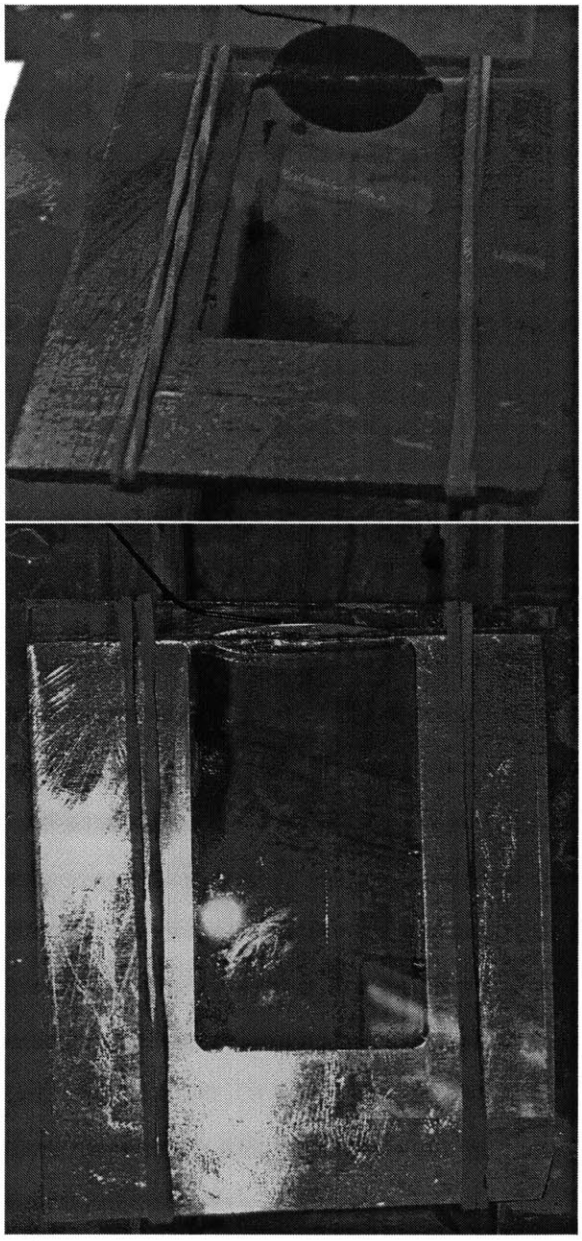

Figure 3-1: Acoustic Cavity Prepared with Bead Stock Solution. The piezoelectric disc is pressed onto the five thousandths of an inch thick membrane of the steel cavity. An ABS depressor held in place by rubber bands ensures consistent coupling. Coverslips are adhered to the top and the bottom of the cavity using vacuum grease. The cavity is filled with bead stock highly diluted in deionized water.

design was of sufficient length for the generation of low frequency acoustic standing waves along the cavity's length. Treating the steel walls as hard reflectors, the first lengthwise mode is at 17.1 kHz, well within measurability.

At one end of the cavity is a thin metal membrane 5 thousandths of an inch thick. The membrane was fabricated by milling that edge down to 10 thousandths and carefully sanding the rest. Vacuum grease is used to adhere coverslips to the steel cavity on both the top and bottom. A piezoelectric element is attached to the steel membrane and driven by a Agilent 33220A function generator. First attempts used vacuum grease to adhere the piezo to the channel. In early experiments, the piezo element would shift about when bumped and affect the coupling. Later an ABS depressor was used in conjunction with rubber bands to hold the piezo firmly against the membrane. A small gap was left between the coverslips and the thin membrane to prevent contact with the piezo. This did not seem to allow significant evaporation from the sample. Samples sustained hours of continuous testing with heating from the laser.

The piezoelectric element is a 2 cm diameter disc piezo. The behavior of the piezoelectric used was measured by coupling two elements together, driving one and measuring the other's response on an oscilloscope. The first resonance of the piezo was around 140 kHz. The response below this resonance is effectively flat. I did not attempt to correct out variations in the piezo response over the spectrum.

3.2 Spectral Analysis of Driven Bead

In this section I demonstrate the optical trap's ability to measure acoustic disturbances. The cavity is driven at a particular frequency below 50 kHz and a spectral analysis is performed on calibrated QPD data. The norm of the trajectory is then multiplied by a stiffness and frequency dependent factor to account for the dynamics of the bead:

$$\left[\left(\frac{k - m\omega^2}{\beta}\right)^2 + \omega^2\right]\langle \mathbf{x}^2 \rangle = \langle \mathbf{v}^2 \rangle . \tag{3.1}$$

Figure 3-2 is an example spectrum with the cavity driven at 17 kHz. For this run,

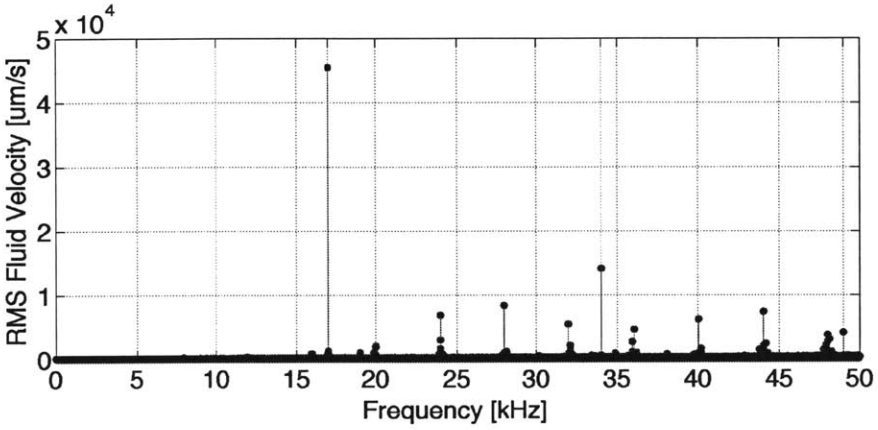

Figure 3-2: Bead Driven at 17 kHz. A 5 V, 17 kHz sinusoidal voltage is supplied to the piezoelectric acoustic source. A DFT of the calibrated QPD data is shown with an acoustic signal to thermal noise ratio on the order of 100. In addition to the 17 kHz peak, two higher order peaks are generated at 34 kHz and 49 aliased from 51 kHz.

data were collected at 100 kHz over 10 seconds, driving the piezo with a sinusoid 5 V_{pp} at 17 kHz. The bead was placed 15 bead diameters from the coverslip halfway along the length of the cavity. The signal peak has an amplitude of 4.5×10^4 μm/s whereas nearby noise fluctuates about 100 μm/s. In the next section we observe smaller driving amplitudes (piezo driven with sinusoid of amplitude 50 mV_{pp}, 100$\times$ smaller than this run). In addition to the peak at 17 kHz, there are diminishing peaks at multiples of 17: one at 34 kHz and one at 49 kHz aliased from 51 kHz.

There is a comb of peaks that arise every 4 kHz. These peaks appear in undriven data sets (Figure 3-4). They do not behave resonantly in that response to driving the piezo about these peaks increases their height by amounts consistent with nearby responses.

The main driving signal is mixed with 60 Hz noise. Sidebands are evident in Figure 3-3.

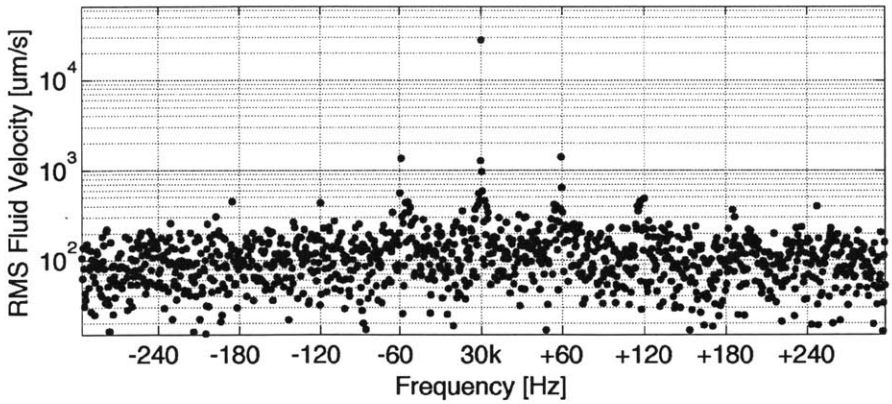

Figure 3-3: 60 Hz Sidebands for Bead Driven at 30 kHz. Nonlinearities give rise to sidebands from mixing acoustic waves generated by the piezo with 60 Hz noise.

3.3 Measuring Cavity Modes

3.3.1 Locating the Modes

In order to find the cavity resonances, the frequency of the voltage across the piezo was swept linearly from 100 Hz to 45 kHz with a fixed amplitude of 5 mV_{pp}. A bead is trapped and placed three quarters of the way down the channel away from the piezo. The resulting spectrum is shown in Figure 3-4 in gray plotted under an undriven spectrum in light red. Of particular interest to us are the peaks at 19 and 38 kHz. They are highlighted on the figure with arrows. As they are near anticipated mode frequencies and multiples of each other, these are likely candidates for standing waves in the cavity.

In a first attempt to measure spatial variations of these peaks, a center frequency for the 19 kHz peak was selected and data was collected at points along the length of the cavity. Repeating the measurements yielded entirely different results. It was at this point that the ABS depressor was used to secure the piezo to the metallic membrane at the entrance to the cavity. Another set of measurements admitted equally irrepeatable results.

A different approach was then taken. Rather than drive the cavity at a particular frequency, a small range about the frequency of interest was swept. Figure 3-5 shows

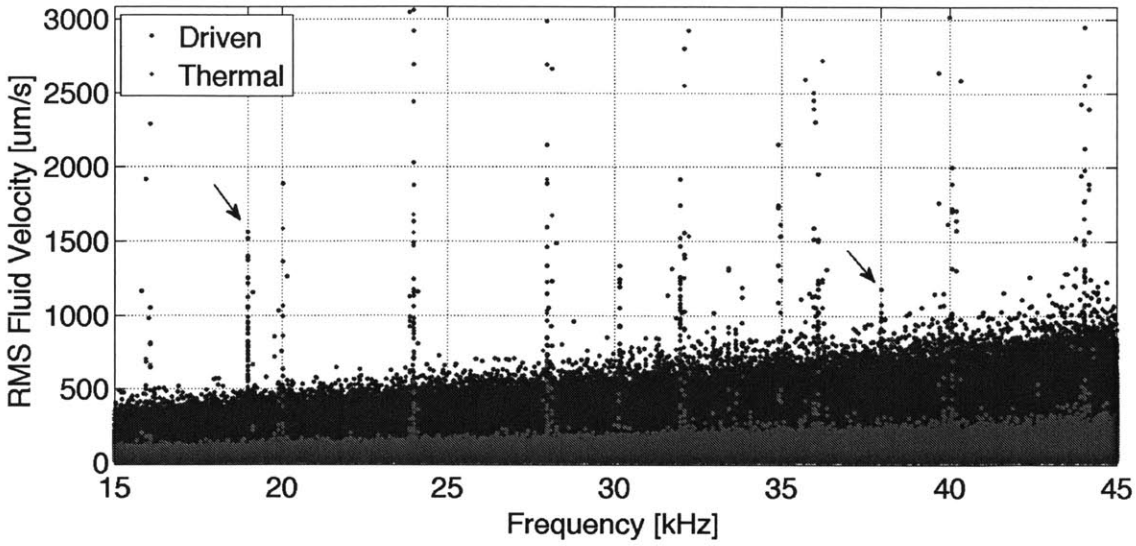

Figure 3-4: Sweep over Driving Frequencies for a Bead at 3L/4 from the Piezo. The frequency of the sinusoidal voltage driving the piezo is swept linearly from 100 Hz to 45 kHz. A DFT of the calibrated QPD data shows a 19 and 38 kHz acoustic cavity resonance. Non-acoustic peaks appear every 4 kHz.

the results of three sweeps of the driving frequency plotted on the same axes. These three runs were taken five minutes apart from each other. The bead was not moved during these measurements. The first run is in black, the second in red, and the third in gray. This shows a slow shift in the peak's center frequency over 10 Hz, or a part in 2000. The 4 kHz separated peak comb does not exhibit this behavior.

These drifts in center frequency fall in the range of feasible fluctuations in the temperature of the fluid medium. The speed of sound increases by about 0.18 %/K. An increase in the fluid's temperature by just 0.3 K can explain the increase in center frequency found in Figure 3-5. This change in temperature could be due to heating by the laser, a hypothesis which is consistent with the observed increase center frequency with time. With further study, this effect could be used for sample thermometry.

3.3.2 Measuring the Height of Modes

Although the center frequency of the cavity mode varies with time, does the size of the resonance stay the same? A metric of the height of a resonant peak that is

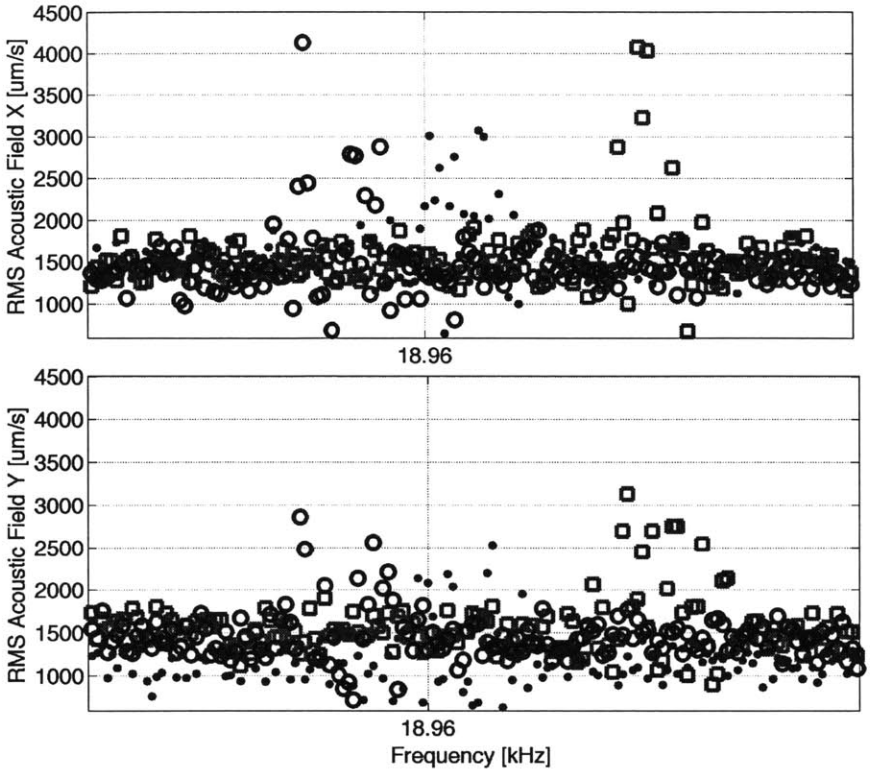

Figure 3-5: Variation of Acoustic Mode Frequency with Time. Data is collected at a fixed location for three ten second intervals separated by five minutes. Here we show the 10 Hz shift in the location of the 19 kHz cavity resonance. This shift is understood in terms of changes of the speed of sound of the medium with temperature.

insensitive to changes in sample temperature and resulting change in center frequency is needed to map the spatial dependence of a standing wave. All tested statistical estimators showed variations in peak size across the runs plotted in Figure 3-5 that are comparable to measured spatial variation in the 19 kHz cavity mode.

In this subsection we analyze data from three ten second intervals taken five minutes apart from one another at the same location within the cavity. The frequency of the sinusoidal voltage driving the piezo is swept linearly from 18.9 to 19.0 kHz, an interval containing the peak of interest. The first method for finding peak height is a simple sum of the points lying in the driven band. The QPD data are calibrated, discrete Fourier transformed, multiplied by their complex conjugate, adjusted by the factor in Equation 3.1, and finally summed between 18.9 and 19.0 kHz. The second

	Sum X	Thresh X	Norm X	Sum Y	Thresh Y	Norm Y
0 min	1.47×10^6	6429	4.35	1.51×10^6	8335	5.52
5 min	1.38×10^6	5820	4.21	1.42×10^6	10744	7.55
10 min	1.50×10^6	9055	6.05	1.19×10^6	12812	10.78

Table 3.1: Discrepancies amongst various statistical estimators for peak height in $\mu m^2/s^2$. Three runs spaced by 5 minutes along both axes suggest acoustic source instability. The three methods, abbreviated Sum for method 1, Thresh for 2, and Norm for 3 are described in this section.

method subtracts out a threshold from the dynamics-corrected spectrum and sums positive points within the band. The threshold for each run is the sum of the mean and 0.2 times the difference between the max and the mean within the band. As can be seen in Figure 3-5 or in the Sum column of Table 3.1, the mean signal within the band does not remain constant. The third method takes the result of the second and normalizes by the mean within the band. The results are shown in Table 3.1.

It is apparent from Table 3.1 that no estimator gives results consistent within 10% for peak size. Perhaps though, variations along the length of the cavity will be much larger than temporal variations. Figure 3-6 shows plots of the three estimators described above along the length of the channel. Variations along the channel are erratic for all three estimators and differ in magnitude comparable to differences exhibited by the fixed-location samples of Figure 3-5.

The erratic behavior of the bead's response amongst the various runs is likely due to instability of the source of acoustic disturbances. Further work necessitates more careful control of acoustic excitations. A next step in the generation and characterization of standing waves in our optical trap is likely the incorporation of feedback control over the piezoelectric source element. A more careful understanding of the behavior of the piezo would contribute to a more complete picture of the dynamics of the cavity; the acoustics throughout the medium could be measured using the trap and the source would be well understood leaving only the behavior of the metal cavity unmeasured.

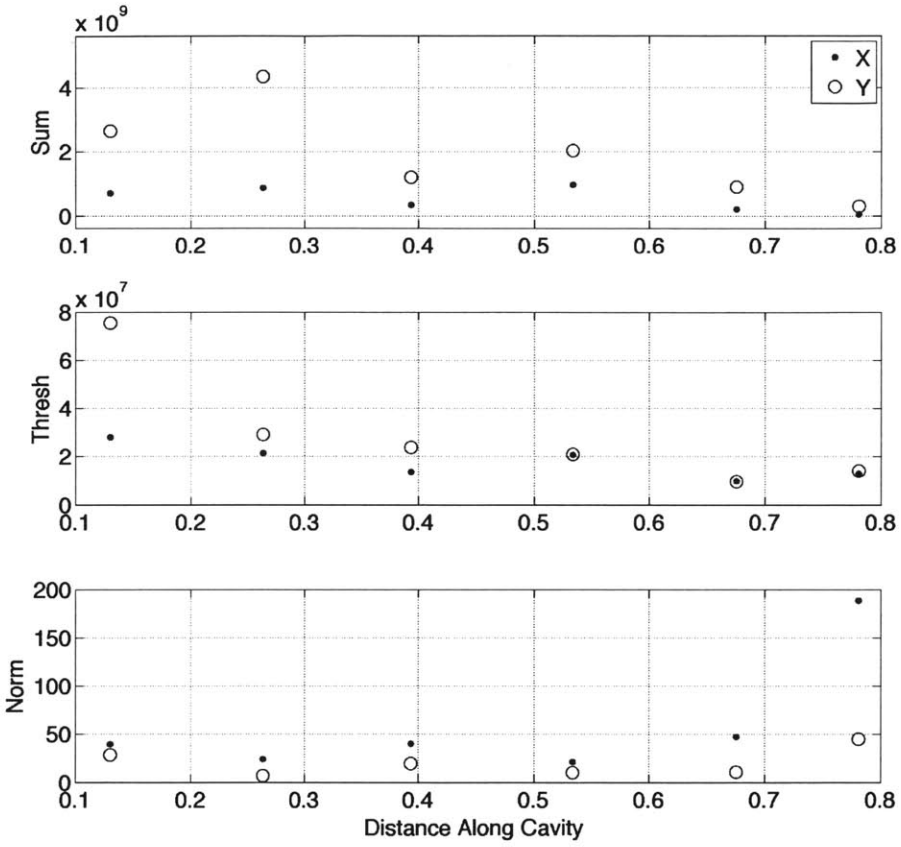

Figure 3-6: Variation of Numerical Integrals along the Sample. No clear trend in the data is evident. Differences amongst points are comparable to the temporal variations of Table 3.1. Lengths along the X-axis are normalized by the cavity length, and 0 denotes the far end of the cavity away from the membrane.

Chapter 4

Conclusion

The apparatus limitations on measurable frequencies of acoustic disturbances is discussed in Chapter 2. For our apparatus, the first constraint is the 50 kHz Nyquist limit of our data acquisition system. This is then followed by diffusion times for electron-hole pairs in the quadrant photodiode. Both problems are easily avoided. Detectors with an order of magnitude greater bandwidth are commercially available. For frequencies beyond this, a separate visible light position-detection beam is necessary.

In preparing for measurements of acoustics, I have more fully characterized our optical trap. This process is described in Chapter 2. High eccentricity was measured in statistical distributions of a trapped object's position at thermal equilibrium. After decorrelating motion along the axes via rotation, a spectral analysis was used to show that the eccentricity was a result of a large, directional 60 Hz noise peak. This noise source falls below the roll off the dynamics and therefore has a large effect on the apparent motion of trapped objects. With an understanding of the effects of this noise source, the trap was characterized through a variety of analyses on thermal and driven measurements. The results are shown in Figure 2-10.

Investigations into the use of optical traps for the measurement of acoustic fields is discussed in Chapter 3. An acoustic cavity capable of supporting two modes below 50 kHz, was constructed with care to ensure strong coupling between the piezoelectric acoustic source and the cavity. The optical trap's sensitivity to acoustic disturbances

in a fluid was demonstrated. Evidence was collected of processes giving rise to higher order signals (Figure 3-2) and mixing with 60 Hz noise (Figure 3-3). Cavity modes were identified and motion of their center frequencies over the course of minutes was observed. This effect is readily explained by variation in the speed of sound in the medium with temperature. With further exploration, this could be used for sample thermometry.

Measurements of the height of cavity mode resonant peaks are discussed. Inconsistent and irrepeatable results for a variety of statistical estimators of peak height suggest instability of the acoustic source. This inconsistency prohibits measurements of spatial variation of acoustic standing waves in the cavity. Efforts to regulate the response of the acoustic source are necessary for further investigation of an optical trapping scheme's application to the measurement of acoustic fields within a fluid medium.

Bibliography

[1] DC Appleyard, KY Vandermeulen, H Lee, and MJ Lang. Optical trapping for undergraduates. *American Journal of Physics*, 75(1):5–14, 2007.

[2] A. Ashkin. Acceleration and Trapping of Particles by Radiation Pressure. *Physical Review Letters*, 24:156–159, January 1970.

[3] Diego Baresch, Jean-Louis Thomas, and Régis Marchiano. Three-dimensional acoustic radiation force on an arbitrarily located elastic sphere. *The Journal of the Acoustical Society of America*, 133(1):25–36, 2013.

[4] Kirstine Berg-Sørensen, Lene Oddershede, Ernst-Ludwig Florin, and Henrik Flyvbjerg. Unintended filtering in a typical photodiode detection system for optical tweezers. *Journal of Applied Physics*, 93(6):3167–3176, 2003.

[5] Steven Chu, J. E. Bjorkholm, A. Ashkin, and A. Cable. Experimental observation of optically trapped atoms. *Phys. Rev. Lett.*, 57:314–317, Jul 1986.

[6] Albert Einstein. Über die von der molekularkinetischen theorie der wärme geforderte bewegung von in ruhenden flüssigkeiten suspendierten teilchen. *Annalen der physik*, 322(8):549–560, 1905.

[7] T. L. Gustavson, A. P. Chikkatur, A. E. Leanhardt, A. Görlitz, S. Gupta, D. E. Pritchard, and W. Ketterle. Transport of bose-einstein condensates with optical tweezers. *Phys. Rev. Lett.*, 88:020401, Dec 2001.

[8] Daisuke Koyama, Hiroyuki Takei, Kentaro Nakamura, and Sadayuki Ueha. A self-running standing wave-type bidirectional slider for the ultrasonically levitated thin linear stage. *Ultrasonics, Ferroelectrics and Frequency Control, IEEE Transactions on*, 55(8):1823–1830, 2008.

[9] Keir C Neuman and Steven M Block. Optical trapping. *Review of Scientific Instruments*, 75(9):2787–2809, 2004.

[10] Erwin JG Peterman, Meindert A van Dijk, Lukas C Kapitein, and Christoph F Schmidt. Extending the bandwidth of optical-tweezers interferometry. *Review of Scientific Instruments*, 74(7):3246–3249, 2003.